Available online at www.sciencedirect.com
ScienceDirect
Trans. Nonferrous Met. Soc. China 30(2020) 3296−3306
Transactions of Nonferrous Metals Society of China
www.tnmsc.cn

Effects of doping route on microstructure and mechanical properties of W−1.0wt.%La_2O_3 alloys

Jun-jun YANG[1*], Gang CHEN[1*], Zheng CHEN[1], Xiao-dong MU[1], Ying YU[1,2], Lin ZHANG[1], Xing-yu LI[1], Xuan-hui QU[1], Ming-li QIN[1]

1. Beijing Advanced Innovation Center for Materials Genome Engineering, Institute for Advanced Materials and Technology, University of Science and Technology Beijing, Beijing 100083, China;
2. Grinm Group Co., Ltd., Beijing 100088, China

Received 15 February 2020; accepted 19 August 2020

Abstract: A comparative study was conducted by using solution combustion synthesis with three different doping routes (liquid−liquid (WL10), liquid−solid (WLNO) and solid−solid (WLO)) to produce nanoscale powders and further fabricate the ultrafine-grained W−1.0wt.%La_2O_3 alloys by pressureless sintering. Compared with pure tungsten, W−1.0wt.%La_2O_3 alloys exhibit ultrafine grains and excellent mechanical properties. After sintering, the average grain size of the WLO sample is larger than that of WL10 and WLNO samples; the microhardness values of WL10 and WLNO samples are similar but larger than the value of WLO sample. The optimized La_2O_3 particles are obtained in the WL10 sample after sintering at 1500 °C with the minimum mean size by comparing with WLNO and WLO samples, which are uniformly distributed either at grain boundaries or in the grain interior with the sizes of (57±29.7) and (27±13.1) nm, respectively. This study exhibits ultrafine microstructure and outperforming mechanical properties of the W−1.0wt.%La_2O_3 alloy via the liquid−liquid doping route, as compared with conventionally-manufactured tungsten materials.

Key words: tungsten alloy; solution combustion synthesis; doping route; ultrafine grain; microhardness

1 Introduction

Tungsten-based materials are very attractive for many engineering applications, such as military, aerospace and nuclear industries owing to their high melting point, high thermal conductivity, high strength at elevated temperatures and low thermal expansion [1−5]. However, their applications are limited due to the well-known embrittlement problems [6−8]. Therefore, it is of great importance to improve their mechanical properties, which are strongly related to the concentration of unavoidable solutes e.g. O, C, P and N [9−12]. However, these impurities are mainly located at grain boundaries (GBs) [13], which weaken the GBs and ultimately lead to brittle failure and deterioration of strength. To date, this problem can be mitigated by modifying grain boundaries and impurity distribution of the tungsten-based alloys. In such a case, the most widely-used pathway is to refine their microstructure [14−16], since it not only

Foundation item: Projects (2017YFB0306000, 2017YFB0305600) supported by the National Key Research and Development Program of China; Projects (51774035, 51604025, 51574031, 51574030, 51574029, 51604240) supported by the National Natural Science Foundation of China; Project (2019JZZY010327) supported by the Shandong Key Research and Development Plan Project, China; Projects (2174079, 2162027) supported by the Natural Science Foundation Program of Beijing, China; Projects (FRF-IDRY-19-025, FRF-TP-17-034A2, FRF-TP-19-015A3, FRF-IDRY-19-003C2) supported by the Fundamental Research Funds for the Central Universities of China
Corresponding author: Ming-li QIN; Tel: +86-10-82377286; E-mail: qinml@mater.ustb.edu.cn
* Jun-jun YANG and Gang CHEN comtributed equally to this work
DOI: 10.1016/S1003-6326(20)65462-0

increases the final strength but creates abundant grain boundaries that can effectively promote the uniformity of impurity distribution and thus the ductility [13]. Therefore, nano-structured tungsten-based materials have been intensively studied in recent years, which exhibit promising results.

The availability of nanoscale tungsten powders is the key point to prepare ultrafine-grained tungsten alloys. There are several effective routes to fabricate nanoscale powders, including hydrothermal synthesis [17,18], co-precipitation processing [19], sol−gel method [20], mechanical alloying [21] and azeotropic distillation [22−24]. Alternatively, we have successfully prepared nanosized tungsten powders by a novel liquid−liquid doping method, i.e. solution combustion synthesis (SCS) [25]. Combined the advantages of wet-chemical synthesis with rapid flame combustion, SCS saves energy and time owing to the abundantly released heat during the short-time processing [26−29], compared with other liquid−liquid doping methods. Particularly, nanoscale rare-earth oxide dispersions (e.g. La_2O_3 [19], Y_2O_3 [20,21] and Pr_2O_3 [30]) doped in the ultrafine-grained tungsten matrix are preferred to gettering impurities due to strong rare-earth−oxygen interactions, which inhibits grain growth by reducing the surface diffusivity of tungsten skeleton [30,31].

Currently, there are three routes to dope the rare-earth oxide particles into refractory metals: (I) Solid−solid (SS). Lu_2O_3 particles could be doped into the tungsten matrix by ball milling to prepare the W−Lu_2O_3 alloy [32]; (II) Liquid−solid (LS). YAR et al [33,34] produced the W−1.0wt.%Y_2O_3 and W−0.9wt.%La_2O_3 nanoscale powders through the reactions in aqueous solutions of yttrium nitrate or lanthanum nitrate with ammonium paratungstate; (III) Liquid−liquid (LL). A sol−gel method was also used to produce W−1.0wt.%Y_2O_3 powders [20]. LIU et al [13] employed the aforementioned three doping routes to fabricate the ultrafine-grained Mo−La_2O_3. They showed that the LL method leads to the most homogeneous and nanoscale microstructure with ultra-high strength and good ductility, since it is processed at a molecular level. However, the commonly-used doping routes are mainly focused on the fabrication of microscale tungsten alloys whose properties should be inferior as compared to the nanoscale-grained tungsten alloys [35]. Additionally, the report on fabricating nanoscale powders and ultrafine-grained tungsten alloys by pressureless sintering as a function of doping route is limited. Furthermore, the comparison of ultrafine-grained tungsten alloys using various doping routes is still lacking either on microstructure or on mechanical properties, as pointed out in a recent review by REN et al [36]. Beyond question, this is beneficial to upgrading the ductility of tungsten alloys.

In this study, we prepared the ultrafine-grained W−1.0wt.%La_2O_3 alloys from house-made nanosized powders using three different doping methods, i.e. LL, LS and SS, followed by pressureless sintering. As such, the purpose of this work is to provide a promising approach to produce high-performance ultrafine-grain tungsten alloys using the three doping routes via pressureless sintering. Besides, the study also focused on the influences of the doping route on the sintering densification, microstructure and mechanical properties.

2 Experimental

Nanoscale tungsten powders doped with 1.0 wt.% La_2O_3 (LL, termed as WL10 hereafter) were made from solution combustion synthesis (SCS) followed by hydrogen reduction, which has been successfully carried out in our previous reports [37−39]. First, the starting materials of 0.01 mol ammonium metatungstate ($(NH_4)_6H_2W_{12}O_4\cdot nH_2O$), 0.24 mol ammonium nitrate (NH_4NO_3), 0.1 mol glycine ($C_2H_5O_2N$) and 0.0014 mol lanthanum nitrate ($La(NO_3)_3\cdot 6H_2O$) were dissolved into the deionized water. A homogeneous solution was achieved by continuous stirring, and then heated until the combustion started. The foamy precursors were obtained after the short-time combustion process, which were subsequently ground into powders. The WL10 powders were fabricated by reducing the SCS-synthesized powders at 700 °C for 2 h under flowing hydrogen. The XRD pattern of the WL10 powders is shown in Fig. 1(a). The SCS-made pure tungsten (PW) powders [25] were mechanically mixed for 4 h with La_2O_3 particles (commercially available with the purity of 99.99% and the D_{50} of ~50 nm) in an anhydrous ethanol medium, termed as WLO hereafter, which is called the SS doping

process. Meanwhile, mixing the SCS-made PW powders [25] with nanoscale La_2O_3 powders via the $La(NO_3)_3$ solution is the LS doping route, called WLNO. Nanoscale La_2O_3 powders with the composition of 1.0 wt.% were doped in the WL10, WLNO and WLO powders, respectively. Figures 1(b) and (c) show the micro-morphologies of the SCS-made pure tungsten powders whose particle size is below 50 nm. Carbon and oxygen levels of the SCS-made tungsten powders are 0.043 wt.% and 1.74 wt.%, determined using a carbon/sulfur analyzer (LECO TC−436) and an oxygen/nitrogen analyzer (LECO CS−444), respectively.

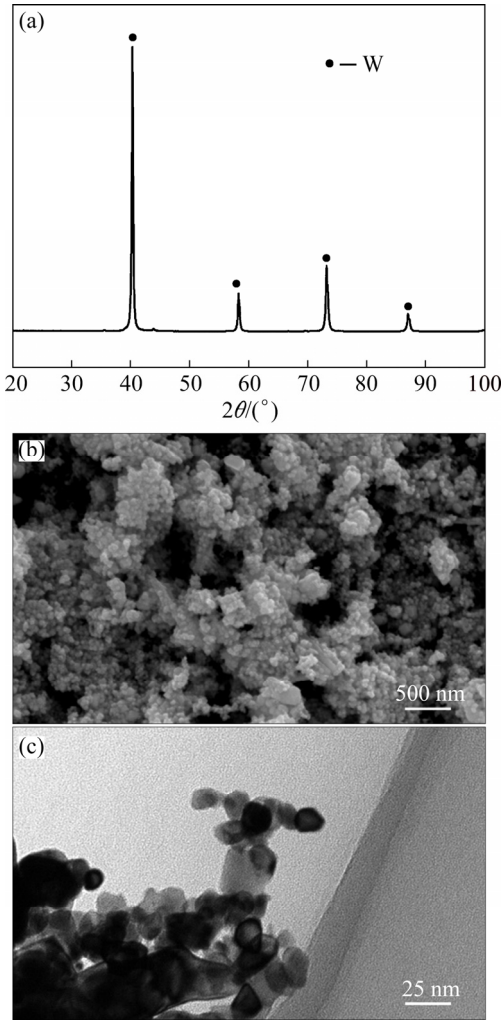

Fig. 1 XRD pattern of WL10 powders (a), and SEM (b) and TEM (c) morphologies of SCS-made nanoscale PW powders

Subsequently, all types of powders with 4 g were pressed into a 15 mm diameter cylindrical die with a uniaxial compaction pressure of 700 MPa holding for 5 s, and then sintered at the final temperatures of 1200, 1350, 1500, 1650 and 1800 °C for 2 h under flowing hydrogen, respectively.

Densities of the as-sintered samples were measured according to the Archimedes principle as per the ASTM B962—14 standard. Microstructures and morphologies of the samples were observed by scanning electron microscopy (SEM, Zeiss LEO−1450) and transmission electron microscopy (TEM, FEI G2), combined with the analysis of selected area electron diffraction (SAED) and energy-dispersive X-ray spectroscopy (EDS). The grain size of the as-sintered samples was quantitatively determined by employing the linear intercept method [40,41] using the particle size analysis software based on SEM images of the fractured samples. The Vickers microhardness test was carried out on the polished samples using a microhardness tester (Leica MH−6) under a 2 N loading at room temperature. Twelve testing readings were used to ensure repeatability in each experiment, and average microhardness values were reported.

3 Results

3.1 Powder morphologies and sintering behavior

Figure 2 shows the TEM images and elemental distributions for all types of powders, i.e. WL10 (Fig. 2(a)), WLNO (Fig. 2(b)) and WLO (Fig. 2(c)), respectively. First, the tungsten powders doped with La_2O_3 particles seem no remarkable difference from the PW powders from the morphological viewpoint by comparing Fig. 2 with Fig. 1. Second, the elemental mapping results indicate that the La_2O_3 particles are homogeneously distributed in the tungsten powder matrix in the case of WL10 and WLNO powders as displayed in Figs. 2(a) and (b), respectively. However, the La in the WLO alloy powders exhibits accumulation (Fig. 2(c)). The results show that both LL and LS doping can realize the uniform distribution of La. The doped tungsten powders demonstrate a similar particle size below 50 nm.

The sintering behavior was investigated and compared as a function of sintering temperature for the samples of PW, WL10, WLNO and WLO. The measured relative density of the green sample with and without doping is similar, i.e. 50%. Figure 3 displays the relative density for each type of sample

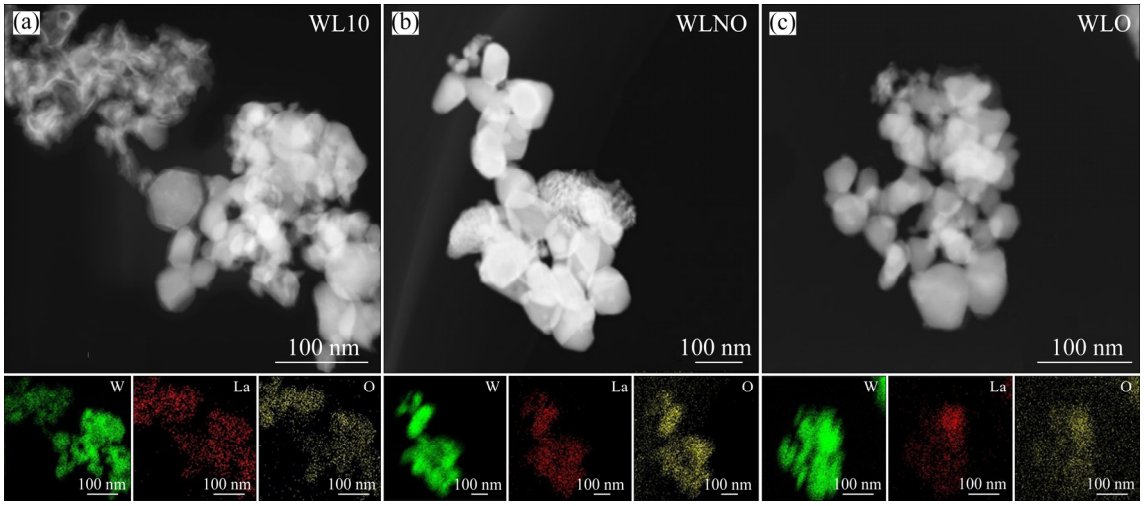

Fig. 2 EDS mapping images at STEM mode for powders of WL10 (a), WLNO (b) and WLO (c)

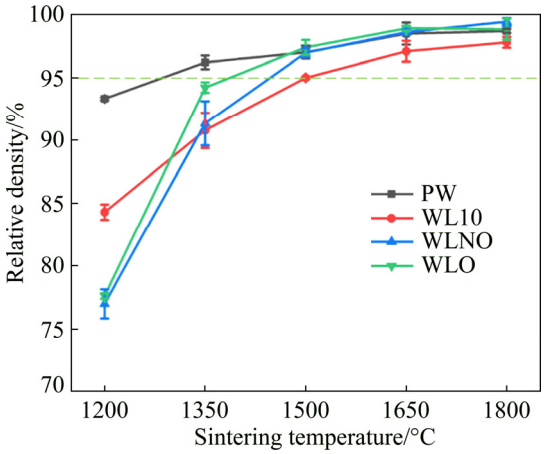

Fig. 3 Relative densities as function of sintering temperature for samples of PW, WL10, WLNO and WLO

after sintering at different temperatures. It can be seen from Fig. 3 that the relative density increases with the sintering temperature for all samples. This is a typical phenomenon in conventional powder sintering, since the atomic diffusion is promoted with increasing the sintering temperature, thus favoring sintering densification. Interestingly, the relative density of the as-sintered PW is at least about 10% higher after sintering at 1200 °C (Fig. 3), beyond which it reaches a relatively constant value, as compared with the three types of doped sample. This is because the doped La_2O_3 particles prevent tungsten powders from sintering densification. However, with further increasing the sintering temperature, all samples after sintering at/above 1500 °C achieve a high relative density above 95.0%, attributed to the enhanced atomic diffusion at high temperatures using the nanosized powders.

3.2 Microstructure

SEM images of the W−1.0wt.%La_2O_3 fabricated using three doping routes (WL10, WLNO and WLO) before and after sintering are illustrated in Fig. 4. It seems that the initial status of all powder compacts is similar in terms of particle size and porosity (Figs. 4(a)−(c)). After sintering at 1200 °C, particle sintering necking occurs (Figs. 4(d)−(f)), concomitant with densification. With continuous sintering at higher temperatures (i.e. 1500 and 1800 °C), sintering densification is enhanced, while the grain size obviously increases with increasing temperature in all samples as observed in Figs. 4(g)−(l). In particular, the average grain size approaches (0.57±0.19), (0.54±0.17) and (0.60±0.17) μm for the samples of WL10, WLNO and WLO after sintering at 1500 °C as demonstrated in Figs. 4(g)−(i), respectively. However, grain coarsening appears after sintering at 1800 °C for the WLO sintered sample, exhibiting the largest grain size (Figs. 4(j)−(l)).

The average grain sizes for the PW and W−1.0wt.%La_2O_3 samples are shown in Fig. 5(a) as a function of sintering temperature. With the increase of sintering temperature, the average grain sizes of the PW and W−1.0wt.%La_2O_3 alloys gradually increase due to the Ostwald ripening mechanism [13]. The average grain sizes of the W−1.0wt.%La_2O_3 alloys are smaller than that of PW at an identical sintering temperature, because the La_2O_3 particles can refine grains by promoting grain nucleation and hindering its growth. When the sintering temperature is below 1650 °C, there is no difference for all the as-sintered samples in terms of

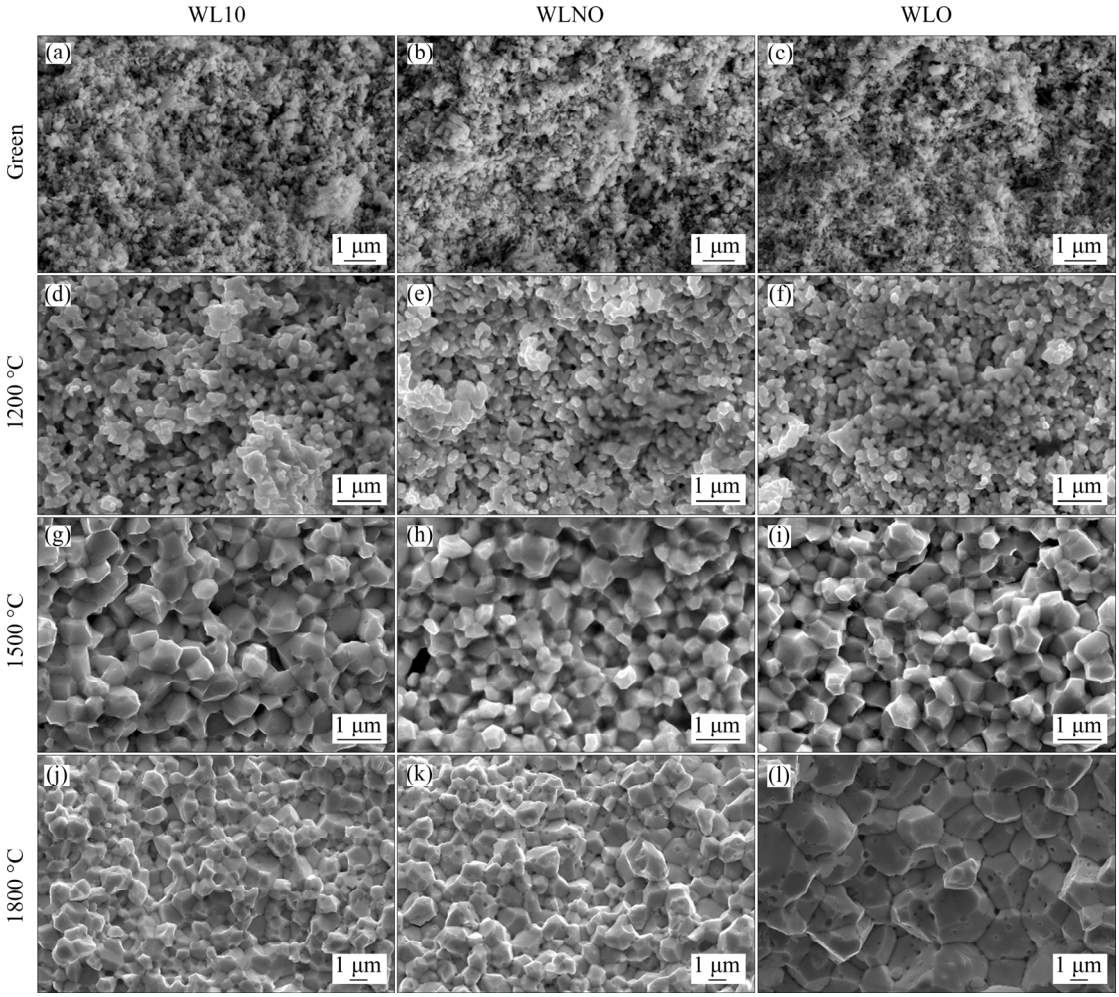

Fig. 4 SEM images of W−1.0wt.%La_2O_3 alloys fabricated using three doping routes as function of sintering temperature

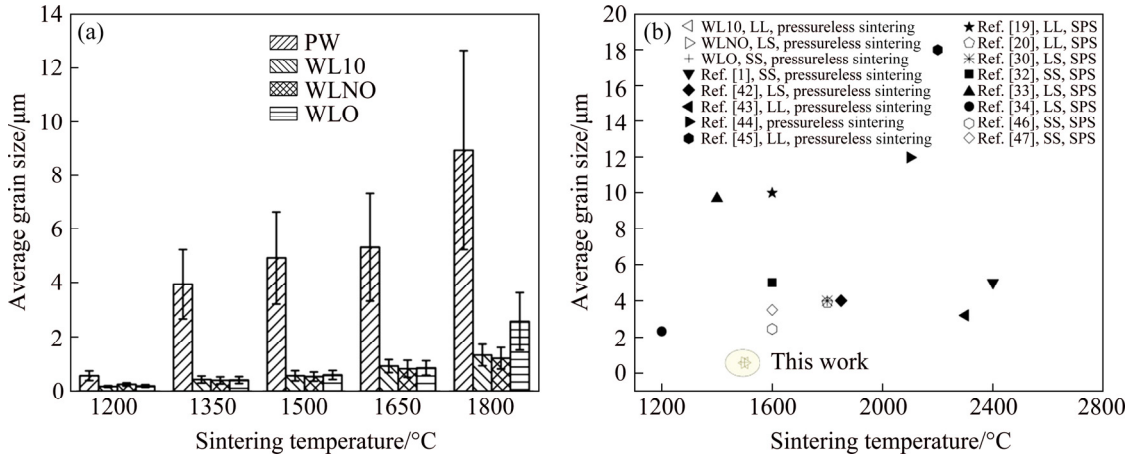

Fig. 5 Average grain sizes for samples of PW and doped W−1.0wt.%La_2O_3 as function of sintering temperature (a) and comparison of average grain sizes as reported in literatures (b)

average grain size. However, when the sintering temperature rises to 1800 °C, the average grain size of the as-sintered WLO sample is larger as compared to those of WL10 and WLNO samples.

The sintered morphological result is consistent with the relative density data in Fig. 3. The result implies that the SCS-made W−1.0wt.%La_2O_3 powder compacts can achieve ultrafine-grained microstructure (grain size below 600 nm) with the relative density above 95.0% after sintering at 1500 °C without assisted pressure. As compared with other reports [1,19,20,30,32−34,42−47] of the

powder-sintered tungsten-based alloys as summarized in Fig. 5(b), this study demonstrates a huge improvement on sintering densification without significant grain coarsening.

TEM images and dispersion particle sizes of the samples (WL10, WLNO and WLO) after sintering at 1500 °C are shown in Fig. 6. The La_2O_3 particles are homogeneously distributed in the tungsten matrix either in the grain interior or at the grain boundary, as observed from the EDS mappings in Figs. 6(a)−(c). The white-colored particles are determined as La_2O_3 under the STEM-HAADF mode and EDS analysis in Figs. 6(d)−(f). The average sizes of the La_2O_3 particles at grain boundaries are (57±29.7), (111±104.6) and (128±37) nm, while the average sizes of the La_2O_3

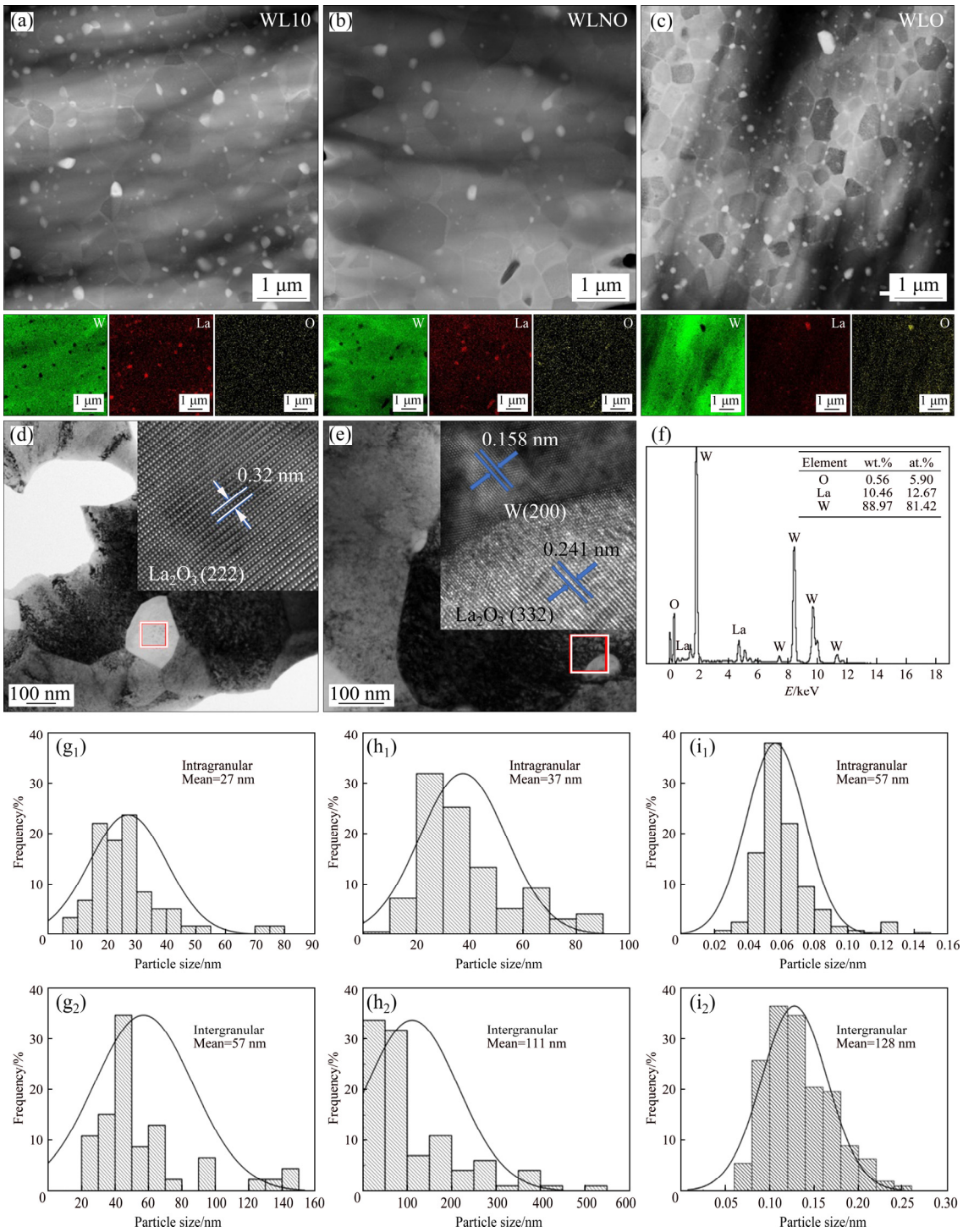

Fig. 6 TEM images, intragranular and intergranular particle size distributions for samples after sintering at 1500 °C: (a, d, g_1, g_2) WL10; (b, e, h_1, h_2) WLNO; (c, f, i_1, i_2) WLO

particles in the grain interior are (27±13.1), (37±16.3) and (57±17.7) nm for the as-sintered WL10, WLNO and WLO samples as shown in Figs. 6(g_1)−(i_2), respectively. Obviously, La_2O_3 dispersions with the smallest size are observed in the sample of WL10, as compared with WLNO and WLO samples. In addition, with the increase of sintering temperature, the particle size of La_2O_3 also grows because of the Ostwald ripening mechanism [13]. The average sizes of the La_2O_3 particles at grain boundaries and in the grain interior for the WL10 are (120±74.4) and (40±18.5) nm after sintering at 1800 °C, respectively.

3.3 Microhardness

To evaluate the effect of the resultant microstructure on the mechanical properties, the microhardness of the as-sintered samples was investigated as a function of sintering temperature as shown in Fig. 7(a). The microhardness of the as-sintered samples increases with increasing the sintering temperature below/at 1500 °C, beyond which it decreases with increasing the sintering temperature (Fig. 7(a)). In other words, the microhardness values reach the maximum values of HV (684.1±14.3), (679.7±43.3) and (650.5±38.6) for the doped samples of WL10, WLNO and WLO after sintering at 1500 °C, respectively. The microhardness for the as-sintered samples of WL10 and WLNO are similar, but slightly higher than that of WLO sample. However, the maximum microhardness is HV (587.1±14.3) after sintering at 1500 °C for the PW sample without doping, much lower as compared with those of the doped samples. The ultrafine-grained tungsten-based alloys in this study using La_2O_3 doping exhibits superior properties as compared with the results in other reports [19,30,32−34,43,46,47] either using pressureless sintering or spark plasma sintering, as summarized in Fig. 7(b). The achieved microhardness values in this case are approximately HV 100 higher than those reported in literatures (Fig. 7(b)), which is mainly due to the ultrafine grains obtained using the SCS-made nanoscale tungsten powders. Therefore, SCS is a promising pathway to produce nanosized powders and ultrafine-grained tungsten-based alloys using pressureless sintering.

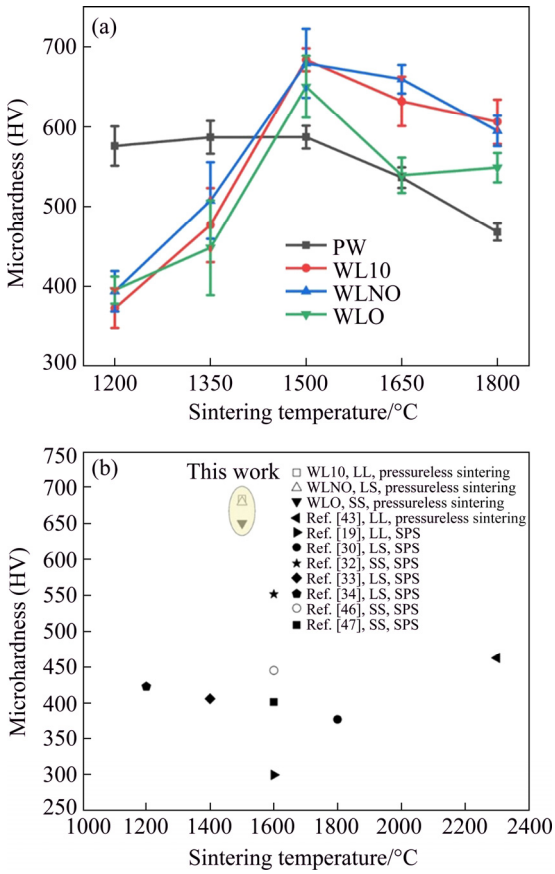

Fig. 7 Microhardness of as-sintered samples of PW and W−1.0wt.%La_2O_3 as function of sintering temperature (a) and comparison of microhardness as reported in literatures (b)

4 Discussion

4.1 Effects of doping on grain size and densification

As shown in Fig. 3, when the sintering temperature is below 1500 °C, relative densities of W−1.0wt.%La_2O_3 are lower than that of PW after sintering. This indicates that the addition of La_2O_3 particles via the three doping routes (LL, LS and SS) hinders sintering densification. This is because oxide particles, dispersed at the grain boundaries, can retard the migration of grain boundaries [16]. As the sintering temperature increases, however, the atomic diffusion increases and thus promotes densification kinetics [40]. Thus, the difference of relative density between the PW and W−1.0wt.%La_2O_3 gradually minimizes when the sintering temperature increases above 1500 °C. Further, with the increase of relative density as well as sintering temperature, the average sizes of tungsten grains and doped particles also grow because of the Ostwald ripening mechanism [13],

as proved in Figs. 4 and 6. The as-sintered sample of WLO exhibits a larger grain size than the WL10 and WLNO after sintering at 1800 °C by comparing Figs. 4(j)−(l). This indicates that grain coarsening is more critical when the doped La_2O_3 particles are likely located at the grain boundaries. In this case, the WLO sample was fabricated from the mechanically-mixed PW and La_2O_3 powders, causing most of La_2O_3 powders located on the tungsten powder surface and thus most likely retained at grain boundaries after sintering. Therefore, the results are totally different from those of the as-sintered samples of WL10 and WLNO. Moreover, the coarsened La_2O_3 particles in the as-sintered sample of WLO are believed to weaken the pinning effect on the grain boundary migration during sintering [48].

4.2 Effects of doping on microhardness

It is well known that the microhardness of materials is correlated to the grain size, relative density, phase constituent, dislocation and secondary phases [13,49,50], etc. In this study, when the sintering temperature is below 1500 °C, the as-sintered PW exhibits a higher microhardness as compared with the doped samples after sintering at an identical temperature (Fig. 7(a)). Nevertheless, this scenario changes after sintering at temperatures above 1500 °C. This can be attributed to the following factors. First, the relative density is much larger for the as-sintered PW sample than that of the doped samples when the sintering temperature is below 1500 °C (Fig. 3). However, with further increasing the sintering temperature, the relative density of the doped samples increases to a similar value with that of the PW sample. Second, the nanoscale La_2O_3 particles act as the dispersion-strengthened role in underpinning the dislocation movement and thus enhancing the microhardness/strength [48,51] when the plastic deformation is carried out. Thus, both density and La_2O_3 dispersions play a dominant role in promoting the final microhardness.

However, the grain sizes of both tungsten matrix and La_2O_3 particles increase with increasing the sintering temperature, although the relative density increases, as observed in Figs. 4 and 6. The microhardness first increases and then decreases with the increase of sintering temperature for all samples (Fig. 7(a)). This is due to the grain size effect on the mechanical properties of materials. We plotted the data of grain size and microhardness from Figs. 4, 6 and 7(a) into Fig. 8 that displays the relationship between the grain size and microhardness of all samples. It seems that the fitting line of relationship is linear as shown in Fig. 8, which obviously agrees well with the Hall−Petch equation of $H_v=H_0+k_H d^{-1/2}$ [8,52], where H_v is the microhardness of the sample, H_0 is the microhardness of single crystal, k_H is a constant, and d is the grain size.

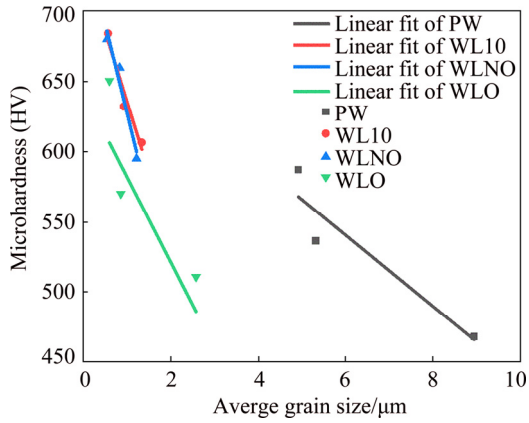

Fig. 8 Relationship between grain size and microhardness of as-sintered PW and W−1.0wt.%La_2O_3 alloys

From the particle sizes of doped La_2O_3 and microhardness of the as-sintered samples in Figs. 4, 6, 7 and 8, it can be concluded that the LL (WL10) and LS (WLNO) doping routes are more beneficial to grain refinement and microhardness enhancement, as compared with the SS (WLO) route. Mechanical properties can be improved by reducing the grain-boundary La_2O_3 particles both in their size and population [13]. A large number of ultrafine La_2O_3 particles are uniformly distributed in the grain interior, while few large La_2O_3 particles are concentrated at grain boundaries for the as-sintered samples of WL10 and WLNO. However, most of the large La_2O_3 particles in the as-sintered sample of WLO are more likely located at grain boundaries, which is prone to produce cracks during plastic deformation. Consequently, the microhardnesses for the as-sintered samples of WL10 and WLNO are similar, but slightly higher as compared with that of WLO.

5 Conclusions

(1) W−1.0wt.%La_2O_3 alloy powders were

prepared by SCS using the LL, LS and SS doping routes. The average particle size is below 50 nm for the as-fabricated WL10, WLNO and WLO doped powders.

(2) After sintering at 1500 °C, the relative density, microhardness, and average grain size are (95.0±0.10)%, (96.9±0.35)% and (97.4±0.59)%; HV (684.1±14.3), (679.7±43.3) and (650.5±38.6); (0.57±0.19), (0.54±0.17) and (0.60±0.17) μm for the as-sintered samples of WL10, WLNO and WLO, respectively.

(3) The as-sintered WL10 sample using the LL doping route exhibits uniformly distributed La_2O_3 particles either at grain boundaries or in the grain interior, and thus demonstrates superior microhardness as compared with the samples of PW, WLNO and WLO.

References

[1] ANTUSCH S, ARMSTRONG D E J, BRITTON T B, COMMIN L, GIBSON J S K L, GREUNER H, HOFFMANN J, KNABL W, PINTSUK G, RIETH M, ROBERTS S G, WEINGAERTNER T. Mechanical and microstructural investigations of tungsten and doped tungsten materials produced via powder injection molding [J]. Nuclear Materials and Energy, 2015, 3−4: 22−31.

[2] LI Ping, SUN Da-zhi, WANG Xue, XUE Ke-min, HUA Rui, WU Yu-cheng. Microstructure and thermal stability of sintered pure tungsten processed by multiple direction compression [J]. Transactions of Nonferrous Metals Society of China, 2018, 28: 461−468.

[3] WANG Kai-fei, ZHANG Guo-hua. Synthesis of high-purity ultrafine tungsten and tungsten carbide powders [J]. Transactions of Nonferrous Metals Society of China, 2020, 30: 1697−1706.

[4] XIAO Fang-nao, XU Liu-jie, ZHOU Yu-cheng, PAN Kun-ming, LI Ji-wen, LIU Wei, WEI Shi-zhong. A hybrid microstructure design strategy achieving W−ZrO_2(Y) alloy with high compressive strength and critical failure strain [J]. Journal of Alloys and Compounds, 2017, 708: 202−212.

[5] HOU Li-zhen, WANG Shi-liang, CHEN Guo-liang, HE Yue-hui, XIE Ya. Mechanical properties of tungsten nanowhiskers characterized by nanoindentation [J]. Transactions of Nonferrous Metals Society of China, 2013, 23: 2323−2328.

[6] WANG Y M, AKTAA J. Microstructure and texture in W and W−1.0wt%La_2O_3 processed by high-pressure torsion [J]. Scripta Materialia, 2017, 139: 22−25.

[7] CHEN Hong-yu, LUO Lai-ma, ZAN Xiang, XU Qiu, TOKUNAGA K, LIU Jia-qin, ZHU Xiao-yong, CHENG Ji-gui, WU Yu-cheng. Thermal shock behavior of W−ZrC/Sc_2O_3 composites under two different transient events by electron and laser irradiation [J]. Journal of Nuclear Materials, 2018, 499: 248−255.

[8] QIAN Chen-hao, HE Zi-yang, LIANG Cheng, JI Wei-xi. Microstructure and hardness of W−25Re alloy processed by high-pressure torsion [J]. Transactions of Nonferrous Metals Society of China, 2017, 27: 2622−2629.

[9] XIE Zhuo-ming, LIU Rui, FANG Qian-feng, ZHANG Tao, JIANG Yan, WANG Xian-ping, LIU Chang-song. Microstructure and mechanical properties of nano-size zirconium carbide dispersion strengthened tungsten alloys fabricated by spark plasma sintering method [J]. Plasma Science and Technology, 2015, 17: 1066−1071.

[10] FUNKENBUSCH A W, BACON F, LEE D. The influence of microstructure on fracture of drawn tungsten wire [J]. Metallurgical Transactions A, 1979, 10: 1085−1091.

[11] LIU R, XIE Z M, HAO T, ZHOU Y, WANG X P, FANG Q F, LIU C S. Fabricating high performance tungsten alloys through zirconium micro-alloying and nano-sized yttria dispersion strengthening [J]. Journal of Nuclear Materials, 2014, 451: 35−39.

[12] WADSWORTH J, NIEH T G, STEPHENS J J. Recent advances in aerospace refractory metal alloys [J]. International Materials Reviews, 1988, 33: 131−150.

[13] LIU G, ZHANG G J, JIANG F, DING X D, SUN Y J, SUN J, MA E. Nanostructured high-strength molybdenum alloys with unprecedented tensile ductility [J]. Nature Materials, 2013, 12: 344−350.

[14] UYTDENHOUWEN I, DECRÉTON M, HIRAI T, LINKE J, PINTSUK G, OOST G V. Influence of recrystallization on thermal shock resistance of various tungsten grades [J]. Journal of Nuclear Materials, 2007, 363−365: 1099−1103.

[15] SMID I, AKIBA M, VIEIDER G, PLÖCHL L. Development of tungsten armor and bonding to copper for plasma-interactive components [J]. Journal of Nuclear Materials, 1998, 258−263: 160−172.

[16] DONG Zhi, LIU Nan, MA Zong-qing, LIU Chen-xi, GUO Qian-ying, LIU Yong-chang. Preparation of ultra-fine grain W−Y_2O_3 alloy by an improved wet chemical method and two-step spark plasma sintering [J]. Journal of Alloys and Compounds, 2017, 695: 2969−2973.

[17] XIAO Fang-nao, MIAO Qiang, WEI Shi-zhong, LIANG Wen-ping, FAN Xiao-man, PAN Kun-ming, XU Liu-jie. Hydrothermal synthesis of nanoplates assembled hierarchical h-WO_3 microspheres and phase evolution in preparing cubic Zr(Y)O_2-doped tungsten powders [J]. Advanced Powder Technology, 2018, 29: 2633−2643.

[18] XIAO Fang-nao, MIAO Qiang, WEI Shi-zhong, BARRIERE T, CHENG Gang, ZUO Shi-wei, XU Liu-jie. Uniform nanosized oxide particles dispersion strengthened tungsten alloy fabricated involving hydrothermal method and hot isostatic pressing [J]. Journal of Alloys and Compounds, 2020, 824: 153894.

[19] XIA Min, YAN Qing-zhi, XU Lei, GUO Hong-yan, ZHU Ling-xu, GE Chang-chun. Bulk tungsten with uniformly dispersed La_2O_3 nanoparticles sintered from co-precipitated La_2O_3/W nanoparticles [J]. Journal of Nuclear Materials, 2013, 434: 85−89.

[20] LIU R, XIE Z M, FANG Q F, ZHANG T, WANG X P, HAO T, LIU C S, DAI Y. Nanostructured yttria dispersion-strengthened tungsten synthesized by sol−gel method [J]. Journal of Alloys and Compounds, 2016, 657:

73−80.

[21] ZHAO Ming-yue, ZHOU Zhang-jian, ZHONG Ming, TAN Jun, LIAN You-yun, LIU Xiang. Thermal shock behavior of fine grained W−Y_2O_3 materials fabricated via two different manufacturing technologies [J]. Journal of Nuclear Materials, 2016, 470: 236−243.

[22] XIAO Fang-nao, XU Liu-jie, ZHOU Yu-cheng, PAN Kun-ming, LI Ji-wen, LIU Wei, WEI Shi-zhong. Preparation, microstructure, and properties of tungsten alloys reinforced by ZrO_2 particles [J]. International Journal of Refractory Metals and Hard Materials, 2017, 64: 40−46.

[23] XU Liu-jie, XIAO Fang-nao, WEI Shi-zhong, ZHOU Yu-cheng, PAN Kun-ming, LI Xiu-qing, LI Ji-wen, LIU Wei. Development of tungsten heavy alloy reinforced by cubic zirconia through liquid−liquid doping and mechanical alloying methods [J]. International Journal of Refractory Metals and Hard Materials, 2019, 78: 1−8.

[24] LI Zhou, XU Liu-jie, WEI Shi-zhong, CHEN Chong, XIAO Fang-nao. Fabrication and mechanical properties of tungsten alloys reinforced with c-ZrO_2 particles [J]. Journal of Alloys and Compounds, 2018, 769: 694−705.

[25] QIN Ming-li, CHEN Zheng, CHEN Peng-qi, ZHAO Shang-jie, LI Rui, MA Ji-dong, QU Xuan-hui. Fabrication of tungsten nano powder by combustion-based method [J]. International Journal of Refractory Metals and Hard Materials, 2017, 68: 145−150.

[26] CHEN Peng-qi, QIN Ming-li, ZHANG De-zhi, CHEN Zheng, JIA Bao-rui, WAN Qi, WU Hao-yang, QU Xuan-hui. Combustion synthesis and excellent photocatalytic degradation properties of $W_{18}O_{49}$ [J]. Cryst Eng Comm, 2015, 17: 5889−5894.

[27] CHEN Peng-qi, QIN Ming-li, CHEN Zheng, JIA Bao-rui, QU Xuan-hui. Solution combustion synthesis of nanosized WO_x: Characterization, mechanism and excellent photocatalytic properties [J]. RSC Advances, 2016, 6: 83101−83109.

[28] LI Fa-tang, RAN Jing-run, JARONIEC M, QIAO Shi-zhang. Solution combustion synthesis of metal oxide nanomaterials for energy storage and conversion [J]. Nanoscale, 2015, 7: 17590−17610.

[29] VARMA A, MUKASYAN A S, ROGACHEV A S, MANUKYAN K V. Solution combustion synthesis of nanoscale materials [J]. Chemical Reviews, 2016, 116: 14493−14586.

[30] DING Xiao-yu, LUO Lai-ma, LU Ze-long, LUO Guang-nan, ZHU Xiao-yong, CHENG Ji-gui, WU Yu-cheng. Chemically produced tungsten-praseodymium oxide composite sintered by spark plasma sintering [J]. Journal of Nuclear Materials, 2014, 454: 200−206.

[31] DONG Zhi, LIU Nan, HU Wei-qiang, KONG Xiang-wei, MA Zong-qing, LIU Yong-chang. The effect of Y_2O_3 on the grain growth and densification of W matrix during low temperature sintering: Experiments and modelling [J]. Materials & Design, 2019, 181: 108080.

[32] ZHANG Jun, LUO Lai-ma, ZHU Xiao-Yong, CHEN Hong-yu, CHEN Jun-ling, ZAN Xiang, CHENG Ji-gui, WU Yu-cheng. Effect of doped Lu_2O_3 on the microstructures and properties of tungsten alloy prepared by spark plasma sintering [J]. Journal of Nuclear Materials, 2015, 456: 316−320.

[33] YAR M A, WAHLBERG S, BERGQVIST H, SALEM H G, JOHNSSON M, MUHAMMED M. Chemically produced nanostructured ODS-lanthanum oxide−tungsten composites sintered by spark plasma [J]. Journal of Nuclear Materials, 2011, 408: 129−135.

[34] YAR M A, WAHLBERG S, BERGQVIST H, SALEM H G, JOHNSSON M, MUHAMMED M. Spark plasma sintering of tungsten−yttrium oxide composites from chemically synthesized nanopowders and microstructural characterization [J]. Journal of Nuclear Materials, 2011, 412: 227−232.

[35] WANG Jin-shu, LAI Chen, LIU Wei, YANG Fan, ZHANG Xi-zhu, CUI Yun-tao, ZHOU Mei-ling. Effect of scandia doping method on the emission uniformity of scandate cathode with Sc_2O_3−W matrix [J]. Materials Research Bulletin, 2013, 48: 3594−3600.

[36] REN C, FANG Z Z, KOOPMAN M, BUTLER B, PARAMORE J, MIDDLEMAS S. Methods for improving ductility of tungsten—A review [J]. International Journal of Refractory Metals and Hard Materials, 2018, 75: 170−183.

[37] QIN Ming-li, YANG Jun-jun, CHEN Zheng, CHEN Peng-qi, ZHAO Shang-jie, CHENG Ji-gui, CAO Peng, JIA Bao-rui, CHEN Gang, ZHANG Lin, QU Xuan-hui. Preparation of intragranular-oxide-strengthened ultrafine-grained tungsten via low-temperature pressureless sintering [J]. Materials Science and Engineering A, 2020, 774: 138878.

[38] CHEN Zheng, QIN Ming-li, YANG Jun-jun, ZHANG Lin, JIA Bao-rui, QU Xuan-hui. Thermal stability and grain growth kinetics of ultrafine-grained W with various amount of La_2O_3 addition [J]. Metallurgical and Materials Transactions A, 2020, 51: 4113−4122.

[39] CHEN Zheng, QIN Ming-li, YANG Jun-jun, ZHANG Lin, JIA Bao-rui, QU Xuan-hui. Effect of La_2O_3 addition on the synthesis of tungsten nano powder via combustion-based method [J]. Journal of Materials Science & Technology, 2020, 58: 24−33.

[40] REN C, FANG Z Z, ZHANG H, KOOPMAN M. The study on low temperature sintering of nano-tungsten powders [J]. International Journal of Refractory Metals and Hard Materials, 2016, 61: 273−278.

[41] WANG X, FANG Z Z, KOOPMAN M. The relationship between the green density and as-sintered density of nano-tungsten compacts [J]. International Journal of Refractory Metals and Hard Materials, 2015, 53: 134−138.

[42] WANG Wei, SONG Jiu-peng, YAN Bin-you, YU Yang. Metal injection molding of tungsten and its alloys [J]. Metal Powder Report, 2016, 71: 441−444.

[43] XIAO Fang-nao, MIAO Qiang, WEI Shi-zhong, LI Zhou, SUN Tie-long, XU Liu-jie. Microstructure and mechanical properties of W−ZrO_2 alloys by different preparation techniques [J]. Journal of Alloys and Compounds, 2019, 774: 210−221.

[44] ZHANG Xiao-xin, YAN Qing-zhi, LANG Shao-ting, WANG Yi-jia, GE Chang-chun. Evolution of hot rolling texture in pure tungsten and lanthanum oxide doped tungsten with various reductions [J]. Materials & Design, 2016, 109: 443−455.

[45] LI Jian-feng, CHENG Ji-gui, WEI Bang-zheng, ZHANG Ming-long, LUO Lai-ma, WU Yu-cheng. Microstructure and properties of La_2O_3 doped W composites prepared by a wet chemical process [J]. International Journal of Refractory Metals and Hard Materials, 2017, 66: 226−233.

[46] ZHAO Ming-yue, ZHOU Zhang-jian, DING Qing-ming, ZHONG Ming, ARSHAD K. Effect of rare earth elements on the consolidation behavior and microstructure of tungsten alloys [J]. International Journal of Refractory Metals and Hard Materials, 2015, 48: 19−23.

[47] ZHU Xiao-yong, ZHANG Jun, LUO Lai-ma, CHEN Jun-ling, CHENG Ji-gui, WU Yu-cheng. Microstructure and properties of W/Sm_2O_3 composites prepared spark plasma sintering [J]. Advanced Powder Technology, 2015, 26: 640−643.

[48] CHEN Xuan, LI Bin, WANG Tao, LI Rui, WANG Juan, REN Shuai, ZHANG Guo-jun. Strengthening mechanisms of Mo−La_2O_3 alloys processed by solid−solid doping and vacuum hot-pressing sintering [J]. Vacuum, 2018, 152: 70−77.

[49] HUANG L, JIANG L, TOPPING T D, DAI C, WANG X, CARPENTER R, HAINES C, SCHOENUNG J M. In situ oxide dispersion strengthened tungsten alloys with high compressive strength and high strain-to-failure [J]. Acta Materialia, 2017, 122: 19−31.

[50] HU Ping, HU Bo-liang, WANG Kuai-she, SONG Rui, YANG Fan, YU Zhi-tao, TAN Jiang-fei, CAO Wei-cheng, LIU Dong-xin, AN Geng, GUO Lei, YU Hai-liang. Strengthening and elongation mechanism of lanthanum-doped titanium−zirconium−molybdenum alloy [J]. Materials Science and Engineering A, 2016, 678: 315−319.

[51] ZAN Xiu-qi, WANG De-zhi, SHI Kai-hua, SUN Ao-kui, XU Bing. Effect of $MoSi_2$/rare earth composite particles on microstructure and mechanical properties of molybdenum [J]. International Journal of Refractory Metals and Hard Materials, 2011, 29: 505−508.

[52] CORDERO Z C, KNIGHT B E, SCHUH C A. Six decades of the Hall−Petch effect — A survey of grain-size strengthening studies on pure metals [J]. International Materials Reviews, 2016, 61: 495−512.

掺杂方法对 W−1.0wt.%La_2O_3 合金显微组织和力学性能的影响

杨军军[1*]，陈 刚[1*]，陈 铮[1]，母晓东[1]，于 瀛[1,2]，章 林[1]，李星宇[1]，曲选辉[1]，秦明礼[1]

1. 北京科技大学 新材料技术研究院 北京材料基因工程高精尖创新中心，北京 100083；
2. 有研科技集团有限公司，北京 100088

摘 要：对采用溶液燃烧合成法并结合不同掺杂方法(液−液(WL10)、液−固(WLNO)和固−固(WLO))制备的纳米尺度粉末及采用常压烧结法制备的超细晶 W−1.0wt.%La_2O_3 合金进行对比研究。与纯钨相比，W−1.0wt.%La_2O_3 合金具有超细晶粒和优异的力学性能。烧结后，WLO 样品的平均晶粒尺寸大于 WL10 和 WLNO 样品的平均晶粒尺寸；WL10 和 WLNO 的显微硬度相差不大，但大于 WLO 的显微硬度。相对于其他样品，在 1500 °C 烧结后的 WL10 样品中 La_2O_3 颗粒呈现最佳分布状态，均匀分布在晶界或晶粒内部，且平均尺寸最小，晶界和晶粒内部的 La_2O_3 颗粒平均尺寸分别为(57±29.7)和(27±13.1) nm。与传统方法制备的钨材料相比，采用液−液掺杂方法制备的 W−1.0wt.%La_2O_3 钨合金呈超细的显微组织和优异的性能。

关键词：钨合金；溶液燃烧合成；掺杂方法；超细晶；显微硬度

(Edited by Wei-ping CHEN)